Materials Science & Engineering A 900 (2024) 146461

Contents lists available at ScienceDirect

Materials Science & Engineering A

journal homepage: www.elsevier.com/locate/msea

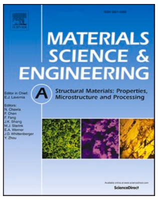

Cryogenic and high temperature tensile properties of 316L steel additively manufactured by laser powder bed fusion

Wengang Zhai [a], Fulin Liu [b], Qingyuan Wang [b], Sharon Mui Ling Nai [c,**], Wei Zhou [a,d,*]

[a] Singapore Centre for 3D Printing, Nanyang Technological University, 50 Nanyang Avenue, 639798, Singapore
[b] Failure Mechanics and Engineering Disaster Prevention Key Laboratory of Sichuan Province, Sichuan University, Chengdu, 610207, China
[c] Additive Manufacturing Division, Singapore Institute of Manufacturing Technology, 5 Cleantech Loop, Cleantech Two Block B, 636732, Singapore
[d] School of Mechanical and Aerospace Engineering, Nanyang Technological University, 50 Nanyang Avenue, 639798, Singapore

ARTICLE INFO

Keywords:
Additive manufacturing
Stainless steel
Stress-induced phase transformation
Twinning-induced plasticity
Dynamic strain aging
Creep

ABSTRACT

316L stainless steel has many industry applications due to its excellent corrosion and oxidation resistance. Laser powder bed fusion (LPBF), a metal additive manufacturing process, is used to fabricate 316L in the current work. Epitaxial grains can be observed in as-built material. LPBF-processed 316L demonstrates both high strength and ductility at room temperature. The yield strength is 609 MPa; the UTS is 722 MPa; the elongation is 62%; LPBF-processed 316L fractured high −196 °C shows an increased strength with good ductility due to transformation induced plasticity (TRIP) and twinning-induced plasticity (TWIP). The yield strength is 818 MPa; the UTS is 1349 MPa; the elongation is 39%. The formation of deformation twinning is significantly retarded when the testing temperature reached 200 °C. At 550 °C and 600 °C, tensile curves with serrated flow were observed which is associated with dynamic strain aging (DSA). Further increasing the testing temperature to 800 °C, the yield strength was decreased to 230 MPa and the UTS was decreased to 239 MPa with an elongation of 29%. Dynamic recrystallization was observed. The short elongation obtained at 800 °C was a result of the occurrence of high temperature creep.

1. Introduction

Austenitic stainless steels have many applications, including food processing, medical instruments, oil and gas, shipbuilding, and aerospace industry, etc., due to their outstanding corrosion and oxidation resistance. 316L, one of the popular grades of austenitic stainless steel, contains 16–18 wt% Cr, 10–14 wt% Ni, and 2–3 wt% Mo. The high content of Cr and Ni results in excellent corrosion and oxidation resistance. The addition of Mo offers 316L acceptable high temperature mechanical properties and further improves its corrosion resistance.

Traditionally, 316L is fabricated using casting followed by a forging process. Small components fabricated with 316L are usually processed using mould forging because of its good formability. Big components are usually processed using milling and welding because of its good machinability and weldability.

Fig. 1 shows the microstructures of a forged 316L. Optical image in Fig. 1(a) and the electron backscatter diffraction (EBSD) orientation map in Fig. 1(b) show its grain morphology. The straight grain boundaries are the Σ3 twin boundaries. The distribution of the Σ3 twin boundaries is highlighted using red lines in Fig. 1(c) which is the grain boundary map obtained using EBSD. The grain boundary misorientation is shown in Fig. 1(d). It can be seen that nearly 50% of the grain boundaries are Σ3 twin boundaries. The formation of twin boundaries is due to its low stacking fault energy of 316L which ranges from 9.1 to 22 mJ/m^2 calculated using different methods [1].

Twin boundaries can be classified into three categories, i.e., growth twin boundaries which are formed during crystal growth; annealing twin boundaries which are formed during recrystallization; and deformation twin boundaries generated by mechanical deformation. The twin boundaries in a forged 316L are the annealing twin boundaries.

Additive manufacturing has been successfully adopted in various industry designs and manufacturing. There are four types of fusion-based metal additive manufacturing processes [2], i.e., laser powder bed fusion (LPBF) which has the highest accuracy, therefore, its advantage is to fabricate components with complex geometry [3]; electron beam powder bed fusion (EBPBF) that the temperature of its

---

* Corresponding author. Singapore Centre for 3D Printing, Nanyang Technological University, 50 Nanyang Avenue, 639798, Singapore.
** Corresponding author.
E-mail addresses: mlnai@simtech.a-star.edu.sg (S.M.L. Nai), mwzhou@ntu.edu.sg, wzhou@cantab.net (W. Zhou).

https://doi.org/10.1016/j.msea.2024.146461
Received 25 September 2023; Received in revised form 9 March 2024; Accepted 4 April 2024

building chamber can be elevated to about 1100 °C, therefore, materials with high tendency of cracking can be fabricated using EBPBF [4]; laser metal deposition (LMD) that has high deposition rate and good accuracy [5]; and wire arc additive manufacturing (WAAM) that has the highest deposition rate [6], therefore, its advantage is to build components with large volume.

Currently, the research of LPBF-processed 316L is mainly focused on the relationship of processing-microstructure-properties [7–9], the origin of high dislocation density [10–12], or its corrosion resistance [13,14]. Extensive recent research has shown that 316L fabricated using LPBF has a better mechanical performance in terms of yield strength, ultimate tensile strength and tensile elongation compared with other fusion-based metal additive manufacturing processes. The yield strength of 316L manufacturing using LPBF can be high at 552 MPa [8], 584 MPa [11], 609 MPa [9], and 638 MPa [7]. It has been reported that the LPBF-processed 316L has a high density of dislocations ($1.1–1.2 \times 10^{15}$ m^{-2}) [11,12]. The high dislocation density contributed about 340 MPa to the yield strength, which can be calculated using the Taylor equation, $\Delta\sigma_d = AGb\sqrt{\rho}$. Its average grain size is usually about 30 μm based on high angle grain boundary [15]. According to the Hall-Petch relationship, the stress is calculated as 230 MPa. The theoretical calculated strength from the Tylor equation and Hall-Petch relationship is close to the experimentally observed values. There are also other factors that should be considered, such as Orowan strengthening from the in-situ formed oxide particles [16]. However, the contribution to strength is small due to the small content of the particles.

The elongation of LPBF-processed 316L is usually between 40% and 60% at room temperature, which is similar to a forged 316L [8]. The good ductility of 316L at room temperature is due to the twinning-induced plasticity (TWIP) phenomenon [17,18]. The lower the stacking fault energy is, the easier the formation of the twinning. It would be interesting to know how much the TWIP contributed to the total tensile elongation of 316L.

Stacking fault energy is a function of temperature [19]. The stacking fault energy is larger at a higher temperature. Therefore, the deformation induced twinning can easily happen at room temperature while difficult at high temperatures. It would be important to know the formation of twinning is retained at which temperature. Muhamed et al. [20] studied the tensile tests of a conventional 316L at different temperatures ranging from room temperature to 800 °C. It is shown that the tensile elongation of a forged 316L decreases with the increase in temperature. At 200 °C, the elongation decreases significantly from 66% to 38%. In addition, serrations were observed in the tensile curves of the forged 316L tested at 500 °C and 600 °C. At 800 °C, the tensile elongation was high at 112%.

Since stacking fault energy is a function of temperature, it would be interesting to study the tensile behavior of LPBF-processed 316L at low temperature. Wang et al. [21] studied the mechanical properties of LPBF-processed 316L tested at −196 °C. They found its yield strength is high at 840 MPa and UTS is 1510 MPa which is much higher than at room temperature. The strength enhancement is attributed to deformation-induced phase transformation. Similar results were obtained in LMD-processed 316L by Karthik et al. [22].

It has been reported that serrated tensile curves which are cause by DSA in conventional 316L when tested at temperatures of 500 °C and 600 °C. Additionally, superplasticity has been observed at 800 °C [20]. Currently, research has explored the deformation behaviors of LPBF-processed 316L at various temperatures, including −196 °C [21]

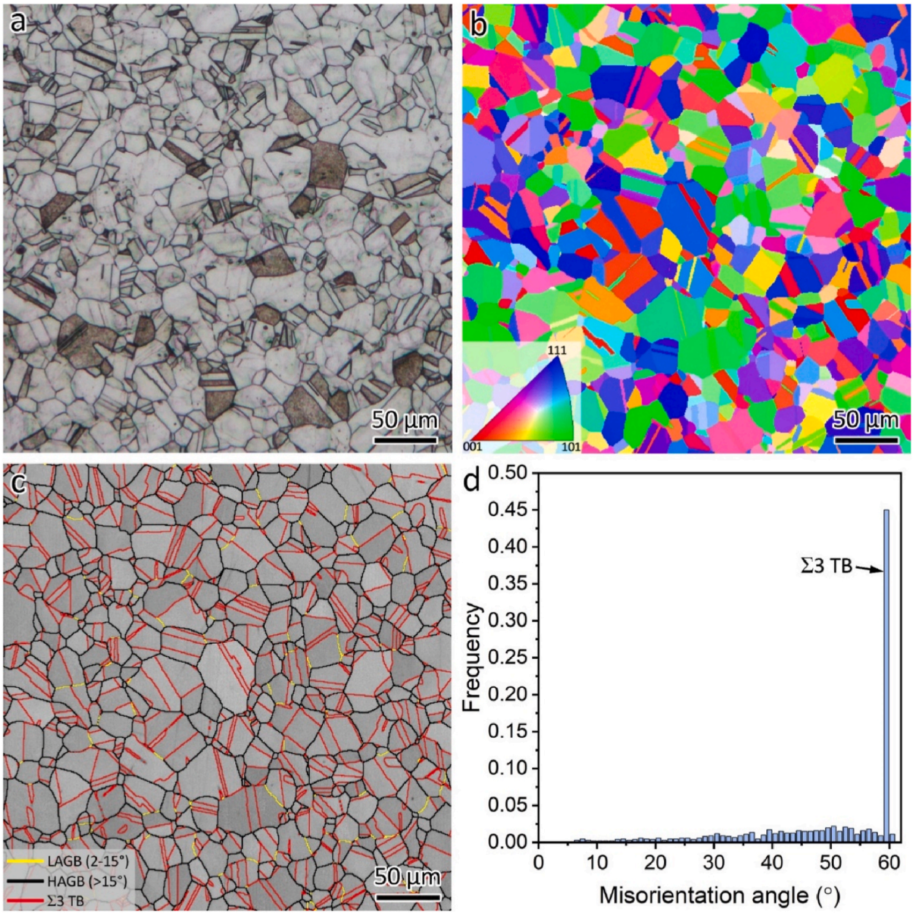

Fig. 1. Microstructures of a wrought 316L. (a) Optical microstructure, (b) EBSD orientation map, (c) grain boundaries map, and (d) grain boundary misorientation distribution. TB: twin boundaries.

and room temperature [23]. However, there remains a gap in understanding the deformation behaviors at high temperatures. Creep, a common phenomenon in metals under mechanical stress, particularly at elevated temperatures, is often influenced by grain boundary morphology [24]. Dynamic recrystallization is another observed behavior in metals subjected to high temperature deformation [25]. LPBF-processed 316L frequently exhibits epitaxial grains, a departure from conventional counterparts. It remains uncertain whether the deformation behaviors observed in conventional 316L would manifest in LPBF-processed 316L. Hence, further investigation is warranted to understand the deformation behaviors across different temperature regimes.

In the current work, the tensile properties of LPBF-processed 316L at different temperatures were investigated. The testing temperatures range from −196 °C to 800 °C. The microstructure evolution of deformed 316L at different testing temperatures has been studied. It has been revealed that at −196 °C, deformation-induced phase transformation and TWIP have been observed; at 25 °C–125 °C, TWIP has been observed; at 550 °C–600 °C, DSA has been observed; at 700 °C–800 °C, creep at grain boundaries have been observed; Moreover, dynamic recrystallization and was observed when tested at 800 °C.

2. Materials and experimental procedures

2.1. Powder feedstock and LPBF printing procedure

Commercial gas-atomized 316L powder with the chemical composition of Fe-16.8Cr-12.7Ni-2.5Mo-1.5Mn-0.7Si-0.011C-0.074O (wt%) was used as feedstock. The mean size of the 316L powder was 42.3 μm measured using a laser scattering machine. The morphology and size distribution of the 316L powder can be found in our previous work [9].

The LPBF machine ProX DMP 300 (3D systems, US) was used to manufacture the 316L samples. The printing machine was integrated with a continuous wave fibre laser (wavelength: 1.070 μm, maximum power: 500 W, and beam diameter at the focal point: 75 μm). Ar gas was used to fill the building chamber to limit the oxygen content to less than 300 ppm. The laser scanning direction was turned 90° to print the next layer. The optimized printing parameters for LPBF of 316L are as follows: laser power 200 W, laser scanning speed 800 mm/s, layer thickness 30 μm, and hatch spacing 70 μm.

2.2. Microstructure characterization

The microstructures were observed using optical microscope, scanning electron microscope (SEM, JEOL 7600F), EBSD (Nordlys, Oxford Instruments), and Transmission Electron Microscope (TEM, JEOL 2100F). X-ray diffraction (XRD) measurement was conducted using Bruker D8 advance machine. The XRD data were analyzed using X'pert Highscore software which contains the Rietveld refinement package.

The LPBF-processed 316L was first ground with progressively finer SiC papers (320–2000 grit). Then silicon oxide polishing suspension (OPS) was used to polish the samples. A self-mixed etching solution (HF: HNO_3: H_2O = 1: 6: 12) was used to etch the samples. The accelerating voltage of 10 kV was used for the SEM observation. XRD was conducted at 40 kV and 40 mA with a 0.6° divergence slit and a step size of 0.02°. EBSD measurements were conducted at the accelerating voltage of 20 kV. The step size of 1.5 μm was used for the measurement of the overall microstructure and a smaller step size of 0.6 μm and 0.1 μm was used for detailed observation. The TEM sample was prepared using ion milling. The accelerating voltage of 200 kV was used for the TEM observation.

2.3. Mechanical properties

Tensile tests were conducted at temperatures of −196 °C, 25 °C, 125 °C, 200 °C, 400 °C, 550 °C, 600 °C, 700 °C, and 800 °C. The tensile test strain rate was 10^{-3} s^{-1}. The tensile machine used was an Instron 5982 universal tensile testing machine. The gauge dimensions of the tensile samples were 14 mm × 4 mm × 2 mm. An electrical discharge machining was used to cut the tensile samples. The tensile strain was recorded using an Instron AVE 2 optical extensometer. Three tensile samples were tested for each condition.

3. Results

3.1. Microstructure LPBF-fabricated 316L

The optical image in Fig. 2(a) shows the melt pool morphology after etching. Hierarchical melt pools can be clearly seen due to the track-by-track and layer-by-layer manufacturing strategy. The melt pools exhibit a semi-elliptical shape. Fig. 2(b) shows the EBSD orientation map of the region b in Fig. 2(a). Fig. 2(c) shows the grain boundaries map obtained using EBSD. The elongated grains cross several layers, which results from the epitaxial growth mode. The direction of the grain growth follows the maximum thermal gradient which is the building direction.

Fig. 2(d) shows the microstructures of the region d in Fig. 2(a). The epitaxial grains can be observed clearly using SEM, as shown in Fig. 2 (d). Submicronsized cellular structures were also observed within the epitaxial grains, as shown in Fig. 2(e). These cellular structures are dislocation cells under TEM, as shown in Fig. 2(f). The high density of dislocations contributes about 300 MPa to the yield strength of LPBF-processed 316L [11,12,26].

Fig. 3 shows the overall microstructures studied using EBSD. Fig. 3 (a) shows the orientation map. Fig. 3(b) shows the grain boundaries map. Fig. 3(c) shows the Schmid factor distribution map. The average Schmid factor was calculated as 0.43. A grain with a higher Schmid factor indicates the grain is easier to reach the critical resolved shear stress. Fig. 3(d) shows the grain boundary misorientation. Compared with the forged 316L (Fig. 1), the main difference is the grain morphology, grain boundaries distribution. LPBF-processed 316L contains a high fraction of low angle grain boundaries (LAGBs, 2–15°), as shown in Fig. 3(d). Although 60° grain boundary misorientation is observed, it is not easy to differentiate the Σ3 twin boundary and the normal 60° grain boundary in LPBF-fabricated 316L.

3.2. Tensile strength of LPBF-processed 316L at different temperatures

The tensile curves of LPBF-fabricated 316L at cryogenic temperature (−196 °C), room temperature (25 °C), and high temperatures (125–800 °C) are shown in Fig. 4. LPBF-fabricated 316L show a good combination of high yield strength and high elongation at room temperature. At room temperature, the yield strength is 609 MPa; and the elongation is 62%.

While tested at −196 °C, the yield strength is 818 MPa which is higher than that at room temperature. The UTS is 1349 MPa and the elongation is 39%. When tested at high temperatures, the yield strength decreases with the increase in testing temperatures. The detailed data of the tensile properties at different testing temperatures are listed in Table 1.

4. Discussion

4.1. Deformation induced martensitic transformation and twinning at −196 °C

In the as-built 316L, only the austenitic phase was detected using XRD, as shown in Fig. 5. Usually, only the austenitic phase is observed in LPBF-processed 316L [12,27,28]. Some studies also observed the presence of a ferritic phase [29]. It mainly depends on the chemical composition and cooling rate [15].

XRD measurement was also conducted for LPBF-processed 316L after tensile test and fractured at −196 °C. Austenitic and martensitic phases were observed, as shown in Fig. 5. The content is 46.1% for austenite

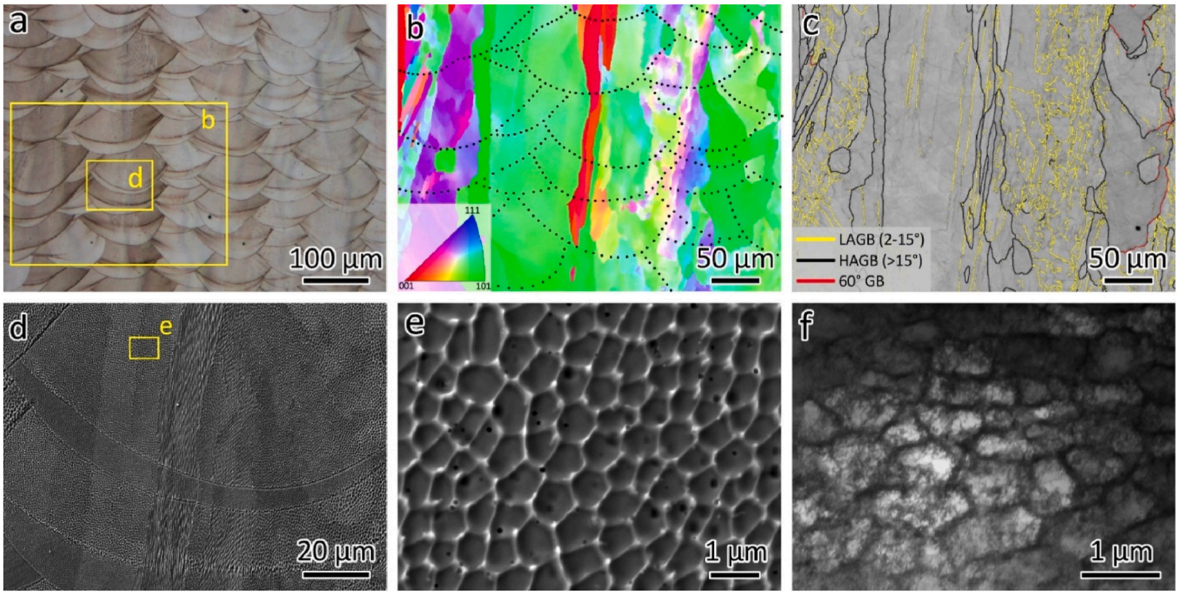

Fig. 2. Microstructures of LPBF-processed 316L. (a) Optical microstructure, (b) EBSD orientation map, (c) grain boundary map, (d) SEM image showing the epitaxial grain growth, (e) SEM image showing cellular structure, and (f) TEM image showing cellular structure.

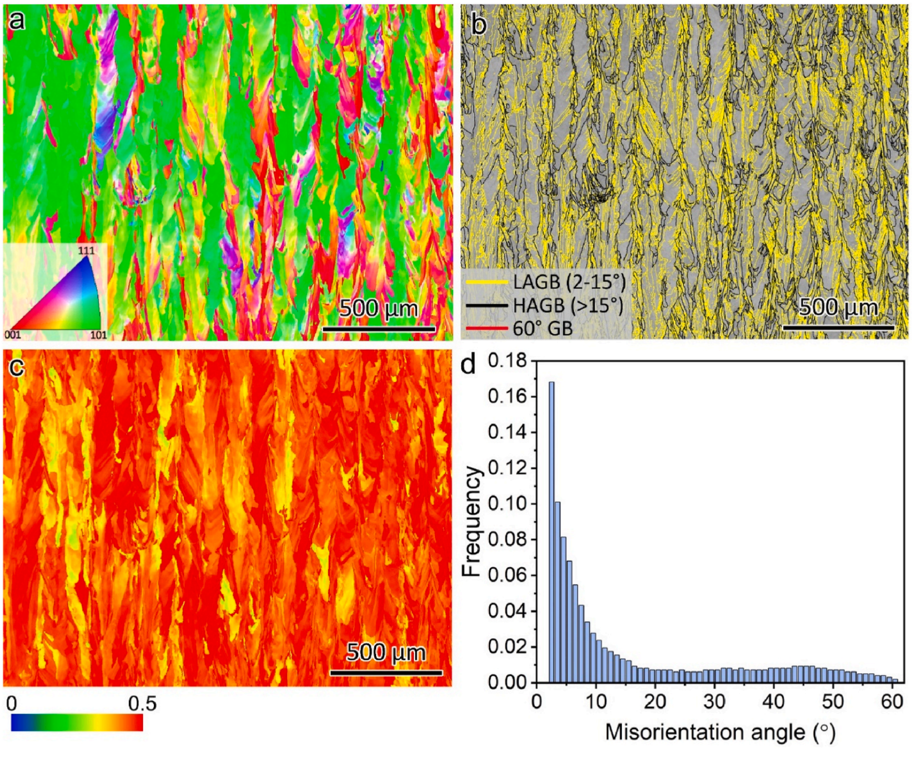

Fig. 3. EBSD study of LPBF-processed 316L. (a) EBSD orientation map, (c) grain boundary map, (c) Schmid factor map, and (d) grain boundary misorientation distribution.

and 53.9% for martensite as analyzed using Highscore software after Rietveld refinement. The martensitic phase was formed due to the deformation induced phase transformation at cryogenic temperature.

The deformation induced martensitic phase transformation is studied using EBSD, as shown in Fig. 6. Fig. 6(a) shows the orientation map and Fig. 6(b) shows the phase map. The retained austenitic phase presents in a strip-like morphology. Due to the severe deformation and high residual stress in the sample fractured at −196 °C, the EBSD index rate is low.

Fig. 7 shows the TEM bright field images of LPBF-processed 316L after tensile test and fractured at −196 °C. The morphology of the deformation induced martensitic phase is shown in Fig. 7(a). A couple of parallel laths with a high density of dislocations were observed in the martensite phase. These laths show a single-crystal diffraction, as shown in the insert of Fig. 7(a) which is a selected area electron diffraction (SAED) pattern with the zone axis of [111]. A similar phenomenon has been observed in the quenching induced martensite [30]. It is known that the deformation induced martensite transformation occurs under

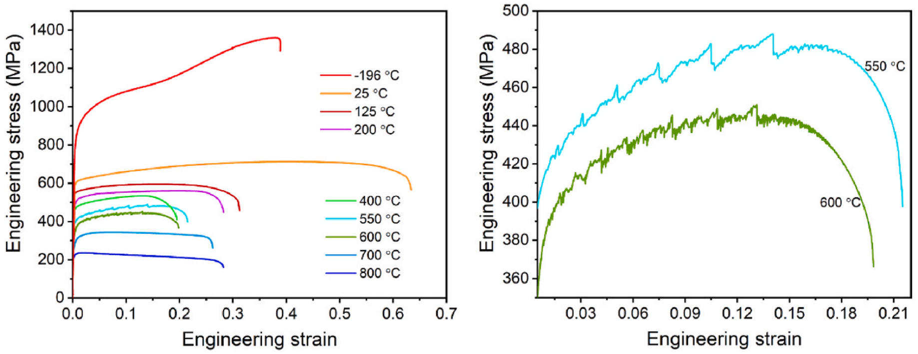

Fig. 4. (a) Tensile curves of LPBF-processed 316L tested at different temperatures, (b) close up of tensile curves at 550 °C and 650 °C showing the serration.

Table 1
Tensile properties of LPBF-processed 316L tested at different temperatures.

	Yield strength (MPa)	UTS (MPa)	Elongation (%)
−196 °C	818 ± 8	1349 ± 11	39 ± 2.8
25 °C	609 ± 9	722 ± 11	62 ± 3.1
125 °C	564 ± 15	605 ± 12	33 ± 2.7
200 °C	480 ± 5	568 ± 10	29 ± 0.3
400 °C	436 ± 16	517 ± 16	21 ± 2.3
550 °C	397 ± 5	488 ± 4	21 ± 0.9
600 °C	363 ± 12	448 ± 3	24 ± 4.7
700 °C	289 ± 8	342 ± 7	28 ± 3.7
800 °C	230 ± 9	236 ± 8	29 ± 2.6

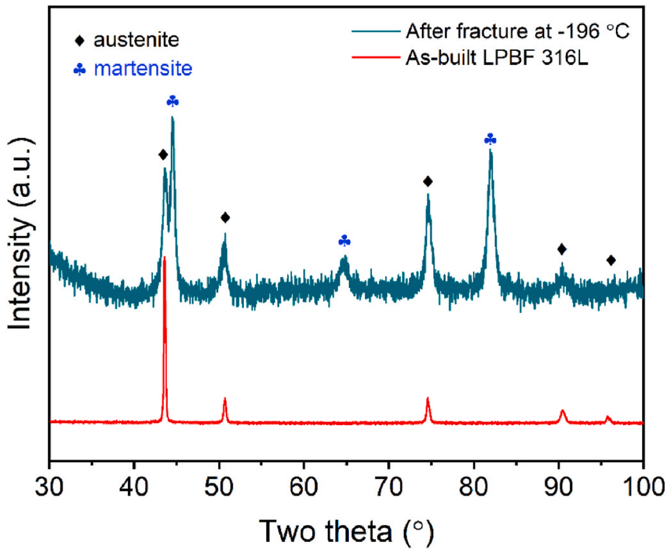

Fig. 5. XRD patterns of as-built 316L and after fractured at −196 °C.

specific defect arrays on {111} planes, which is characterized by the $a/6\langle 11\bar{2}\rangle$ Shockley partial dislocation [31]. The deformation induced martensite is generated by two intersecting shear systems. Huang et al. [32] observed the deformation induced martensite nucleates at the intersection of deformation twins for conventional 316L. Further study needs to be conducted particularly into the mechanism of deformation-induced martensite, with special emphasis on the effect of cellular structure and epitaxial grain morphology of LPBF-processed 316L.

Fig. 7(b) shows another TEM bright field image of LPBF-processed 316L after fractured at −196 °C. The insert in Fig. 7(b) is the corresponding SAED pattern of the deformation twinning. Twinning was not observed using EBSD because of its small width. The SAED pattern in Fig. 7(b) consists of diffraction patterns of the austenite matrix and the twinned austenite. The two sets of diffraction patterns are symmetrical. The twin interface is parallel to {111} planes which have the stacking sequence of …ABCABC …. The stacking sequence of the {111} planes on the other side of the twin boundary is a mirror reflection, so that the sequence across the boundary is … ABCABACBA …. The central B layer represents the boundary between the twin and the matrix.

Fig. 8 shows the progressively magnified SEM backscatter electron (BSE) image of LPBF-processed 316L after fractured at −196 °C. The strip-like morphology of the deformation induced martensite can be seen clearly. The width of the martensite is nanosized. The high elongation of LPBF-processed 316L tested at −196 °C is a combined result of TRIP and TWIP.

4.2. Twinning induced plasticity at room temperature, 125 °C and 200 °C

EBSD studies in Fig. 8 show the microstructures of LPBF-processed 316L fractured at 25 °C, 125 °C and 200 °C. Fig. 8 shows the evolution of the deformation induced twinning.

Fig. 9(a, b, c) show the microstructures after fractured at 25 °C. Fig. 9(a) is the orientation map. Fig. 9(b) shows the grain boundary misorientation distribution. About 13.2% of grain boundaries are $\Sigma 3$ twin boundaries. Fig. 9(c) shows the location of $\Sigma 3$ twin boundaries. Fig. 9(d, e, f) show the microstructures after fractured at 125 °C. Fig. 9(d) is the orientation map. Fig. 9(e) shows the grain boundary misorientation distribution. About 3.8% of grain boundaries are $\Sigma 3$ twin boundaries. Fig. 9(f) shows the location of $\Sigma 3$ twin boundaries. Fig. 9(g, h, i) show the microstructures after fractured at 200 °C. Fig. 9(g) is the orientation map. Fig. 9(h) shows the grain boundary misorientation distribution. About 0.6% of grain boundaries are $\Sigma 3$ twin boundaries. Fig. 8(i) shows the location of $\Sigma 3$ twin boundaries.

With the increase of testing temperature, the content of $\Sigma 3$ twin boundaries decreases significantly. The high content of $\Sigma 3$ twin boundaries deformed at room temperature contributes to the high tensile elongation.

It is noted that the multiple grains in Fig. 9 do not exhibit twinning. The formation of deformation twinning is grain orientation dependent. It has been reported that the deformation twinning occurs preferentially in grains with a Copper orientation ({112}<111>) [33]. A grain with a higher Schmid factor is also preferable for the formation of deformation twin boundary. The value of Schmid factor equals $\cos\varphi \cos\lambda$, where φ is the angle between the direction of applied force and the normal direction of the slip plane, and λ is the angle between the direction of applied force and the slip direction. The resolved shear stress for the activation of the twinning $\tau = \sigma_T \cos\varphi \cos\lambda$, where σ_T is the critical stress for the formation of deformation twinning boundary. Therefore, the formation of deformation twinning is controlled by the grain orientation and Schmid factor simultaneously.

The effect of twining on strengthening is complex. There would be two opposite effects. First, the formation of deformation twin boundary would refine the grains and thus cause a higher grain boundary

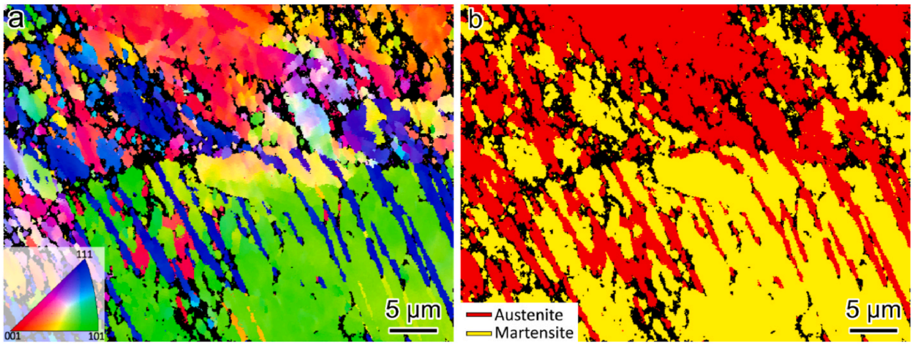

Fig. 6. EBSD results of LPBF-fabricated 316L after fractured at −196 °C. (a) Orientation map, (b) phase map.

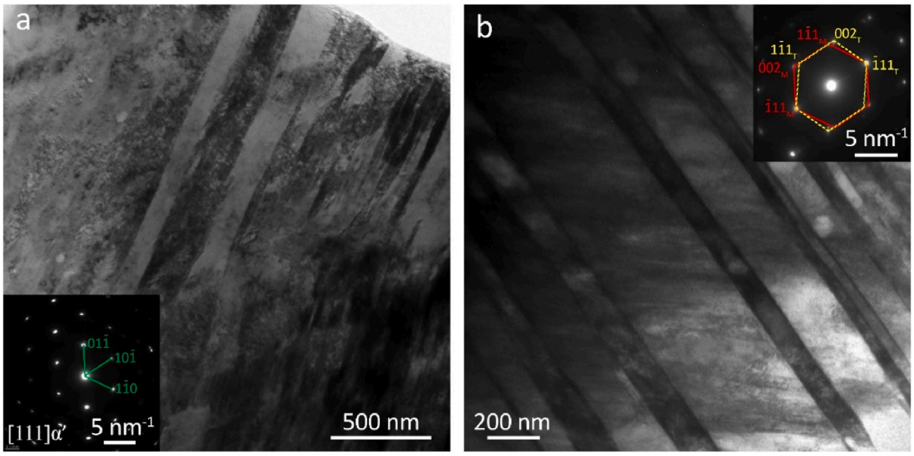

Fig. 7. TEM bright field images showing the deformation induced martensitic phase and twinning of LPBF-processed 316L fractured at −196 °C (a) martensitic phase, (b) deformation twinning. The inserts showing the corresponding SAEDs.

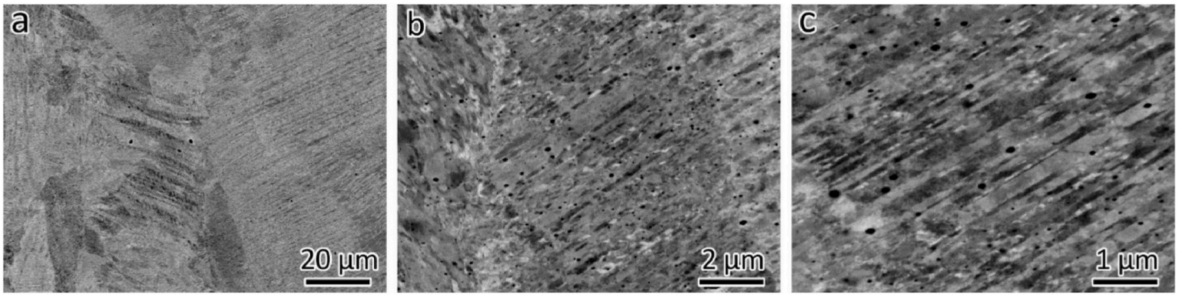

Fig. 8. SEM BSE images with different magnifications showing the microstructures of LPBF-processed 316L fractured at −196 °C.

strengthening. Second, during the tensile test, the stress concentration is released. As reported by Abuzaid et al. [34], a clear stress drop can be observed in the tensile curve of a single crystal FeCrCoMnNi high entropy alloy when twinning occurs. LPBF-processed 316L usually has low strain rate hardening since its tensile curves at room temperature are nearly flat [23,35]. Compared with conventional 316L, deformation twining starts to form at a lower strain for LPBF-processed one [36]. Therefore, it can be concluded that the release of stress concentration is more extensive than grain boundary strengthening.

The content of Σ3 twin boundaries detected using EBSD does not reflect the actual content that the samples possess after the tensile test because nanosized twin boundaries are not detectable. SEM BSE images in Fig. 10 show the nanosized deformation twin boundaries in LPBF-processed 316L fractured at 25 °C. The nanosized twin boundaries intertwin with the slip band, as shown in Fig. 10(b).

4.3. Dynamic strain aging at 550 °C and 600 °C

Fig. 11(a, b, c) show the microstructures observed using EBSD after fractured at 400 °C. Fig. 11(a) is the orientation map. Fig. 11(b) shows the grain boundary misorientation distribution. Fig. 11(c) shows the band contrast map. The EBSD results of LPBF-processed 316L fractured at 550 °C are shown in Fig. 11(d, e, f). The EBSD results for 600 °C are similar to the ones for 500 °C and therefore they are not shown here.

SEM BSE images in Fig. 12 show the microstructures of LPBF-processed 316L fractured at 550 °C. The cellular structure, which is similar to the as-built 316L (Fig. 2(e)), still can be observed.

Interestingly, serrated tensile curves of LPBF-processed 316L were observed when tested at 550 °C and 600 °C, as shown in Fig. 4(b). The serrated flow behavior is named dynamic strain aging (DSA) or Portevin-Le-Chatelier (PLC) effect. There are three main explanations for the

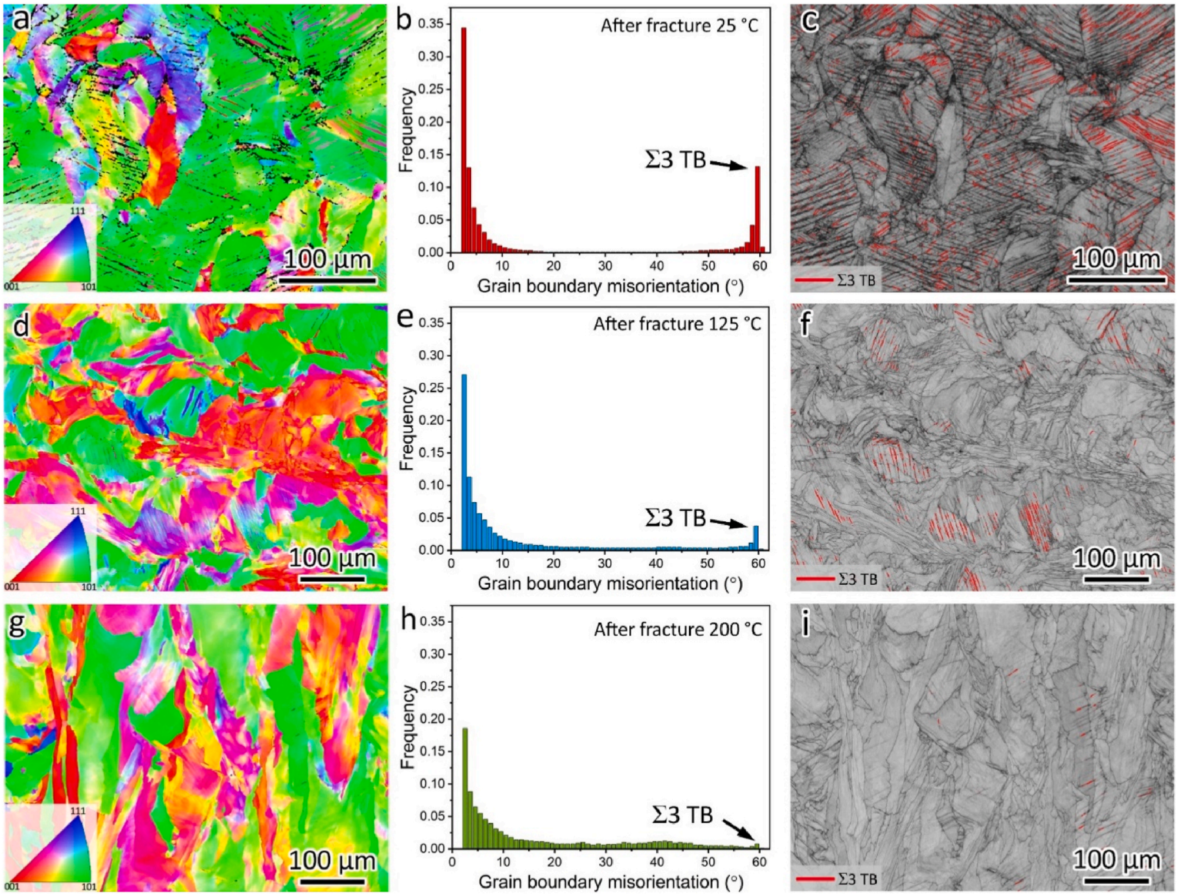

Fig. 9. EBSD studies showing the evolution of deformation twinning of LPBF-processed 316L fractured at (a, b, c) 25 °C, (d, e, f) 125 °C, and (g, h, i) 200 °C. (a, d, g) Orientation map, (b, e, h) grain boundary isorientation distribution, (c, f, i) band contrast map.

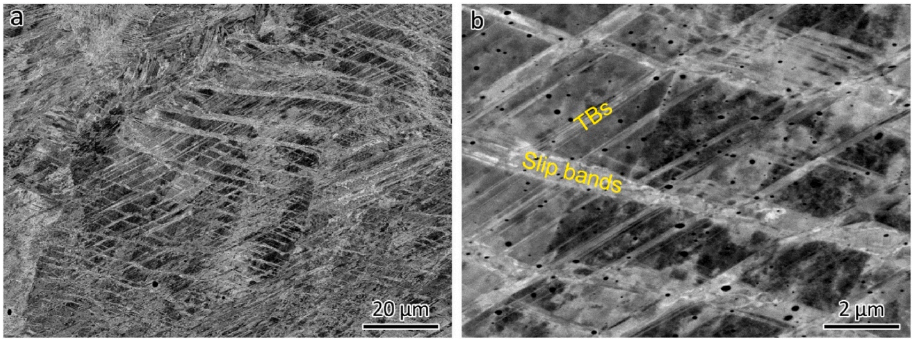

Fig. 10. SEM BSE images with different magnifications showing the deformation twinning in LPBF-processed 316L fractured at 25 °C.

serration behavior, i.e., (i) dynamic interaction between diffusing solute atoms and dislocations; (ii) shearing of precipitates by dislocations; (iii) large group of dislocations move together [37]. The most accepted explanation for the DSA is the first one. It refers to the repeated pinning and breaking of the pinning between diffusing solute atoms and dislocations. The pinning results in the sudden hardening and the breaking of the pinning results in the abrupt softening. There are three types of serrations, type A, B, and C. According to the characteristics [38], the serrations at 550 °C belong to type A and 600 °C is a type A + B.

The DSA phenomenon is associated with flow instability during deformation under specific conditions, such as the presence of solutes, medium strain rate and elevated temperatures. Serrated tensile curves have been frequently observed in the tensile test of low carbon steels at room temperature. It is believed to be the result of the pinning of the moving dislocations with the interstitial atoms, such as carbon and nitrogen. At certain heat treatments, the DSA phenomenon disappeared, especially after high temperature solution treatment [39,40]. Lee et al. [41] studied the effect of strain rate on the DSA of a Fe12Mn0.6C steel. They found that the DSA disappeared when the strain rate increased to 10^{-1} s^{-1}. The DSA phenomenon has also been frequently observed for Aluminum alloys at room temperature [39]. Thus, DSA is an energy-based phenomenon that depends on the activation barriers for the interaction between the solutes and the dislocations.

4.4. Creep and dynamic recrystallization at 800 °C

An interesting phenomenon was observed for LPBF-processed 316L after the tensile test at 800 °C was dynamic recrystallization. Fig. 13(a)

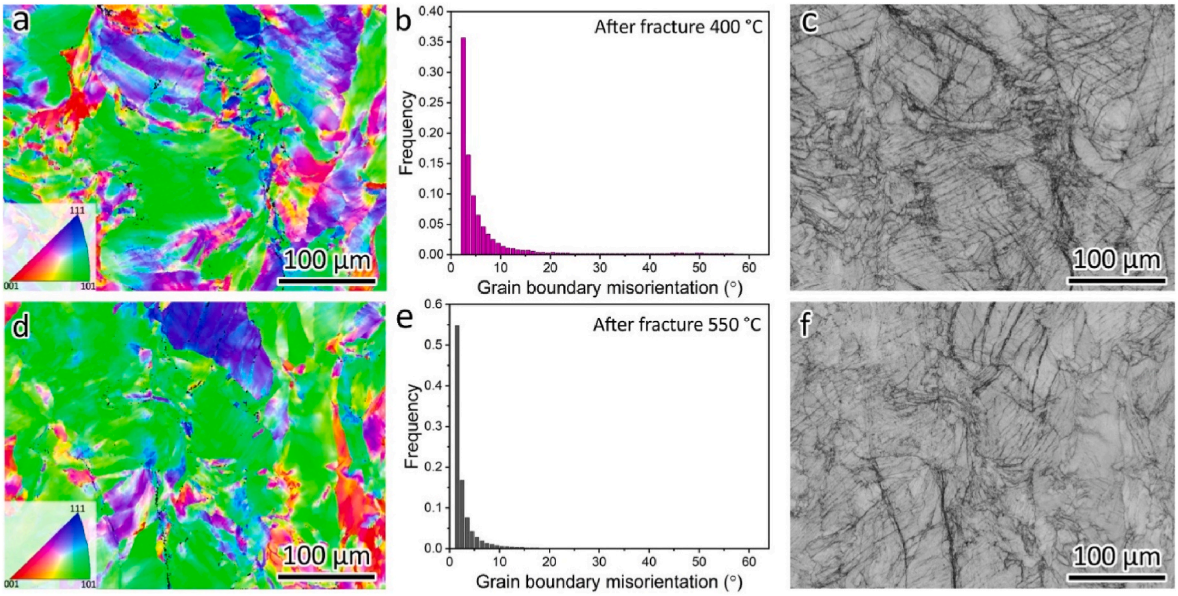

Fig. 11. EBSD studies showing the evolution of deformation twinning of LPBF-processed 316L fractured at (a, b, c) 400 °C, and (d, e, f) 550 °C. (a, d) Orientation map, (b, e) grain boundary misorientation distribution, (c, f) band contrast map.

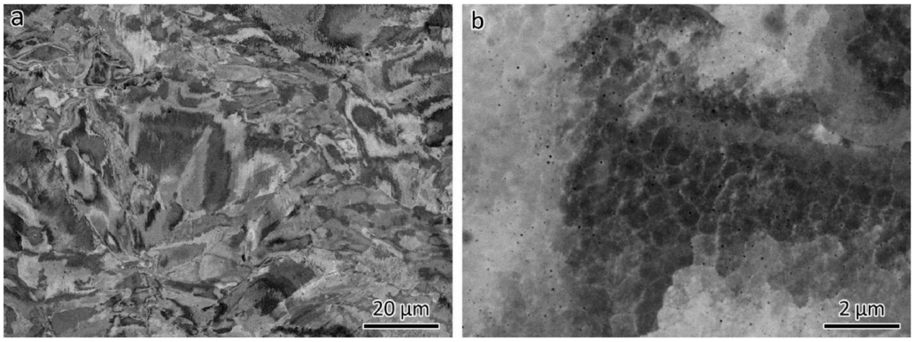

Fig. 12. SEM BSE images with different magnifications showing the microstructures of LPBF-processed 316L fractured at 550 °C.

shows the EBSD orientation map of the fractured sample and a close up is shown in Fig. 13(b). The refined grains due to the dynamic recrystallization can be seen clearly. Fig. 13(c) shows the kernel average misorientation (KAM) map and Fig. 13(d) shows the grain orientation spread (GOS) map which are the same location as Fig. 13(b). The KAM calculates the average misorientation angle between a point and its neighbors, which is an indication of the dislocation density of geometrically necessary dislocations (GNDs). The GOS is a primary strain analysis tool to highlight grains experiencing significant deformation and showcase their spatial distribution. The KAM map reveals the recrystallized grains are surrounded by high amounts of misorientation that act as the driving force. Since the recrystallized grains experience low deformation, the grains are marked with blue color, as shown in Fig. 13(d).

The recrystallized grains were observed using SEM BSE as well, as shown in Fig. 13(c, d, e). The necklaces of new grains form along the initial grain boundaries. The tensile deformation and the high temperature environment offer the motivation for the formation of recrystallized grains. There is no recrystallized grain observed when the testing temperature is 700 °C and below.

316L tested at medium temperatures only shows a relatively small elongation because the formation of deformation twinning is retarded. Conventional 316L tested at 800 °C shows a superplasticity (112%) [20]. The superplasticity is mainly due to the dynamic recrystallization that happens during the tensile test at high temperatures. The formation of recrystallized grains decreases the stress concentration and therefore, the sample can endure more deformation. However, the superplasticity was not observed in LPBF-processed 316L. Further analysis of the fractured sample has been conducted to explore the cause.

Fig. 14(a) shows the optical image of a tensile sample after being tested at 800 °C. Large cavities and cracks can be observed. Some of the cracks were initiated from the sample surface. A close up of the microstructure observed using SEM is shown in Fig. 14(b). Besides the large cavities and cracks, small slim cracks were also observed. The rectangular area c is studied using EBSD and the result is shown in Fig. 14(c). Two slim cracks are shown in Fig. 14(d and e). The location of the two slim cracks is highlighted in Fig. 14(c). The EBSD orientation map confirms that the cracks are along the high angle grain boundaries.

The intergranular cracks are a result of high temperature creep. High temperature creep causes premature fracture and thus the superplasticity was not observed for LPBF-processed 316L at 800 °C. At present, studies on the high temperature creep behavior of LPBF-processed 316L are still limited [42–44]. During the tensile test at 800 °C, the loading direction of the tensile specimens was perpendicular to the direction of the columnar grain growth. In this loading direction, the diffusion path is longer than that along the building direction, which indicates the creep life is shorter than along the building direction. This could be the reason for the observation of large cracks which is parallel to the building direction, as shown in Fig. 14(a). Experimental results reported by Williams et al. [42] proved the above analysis.

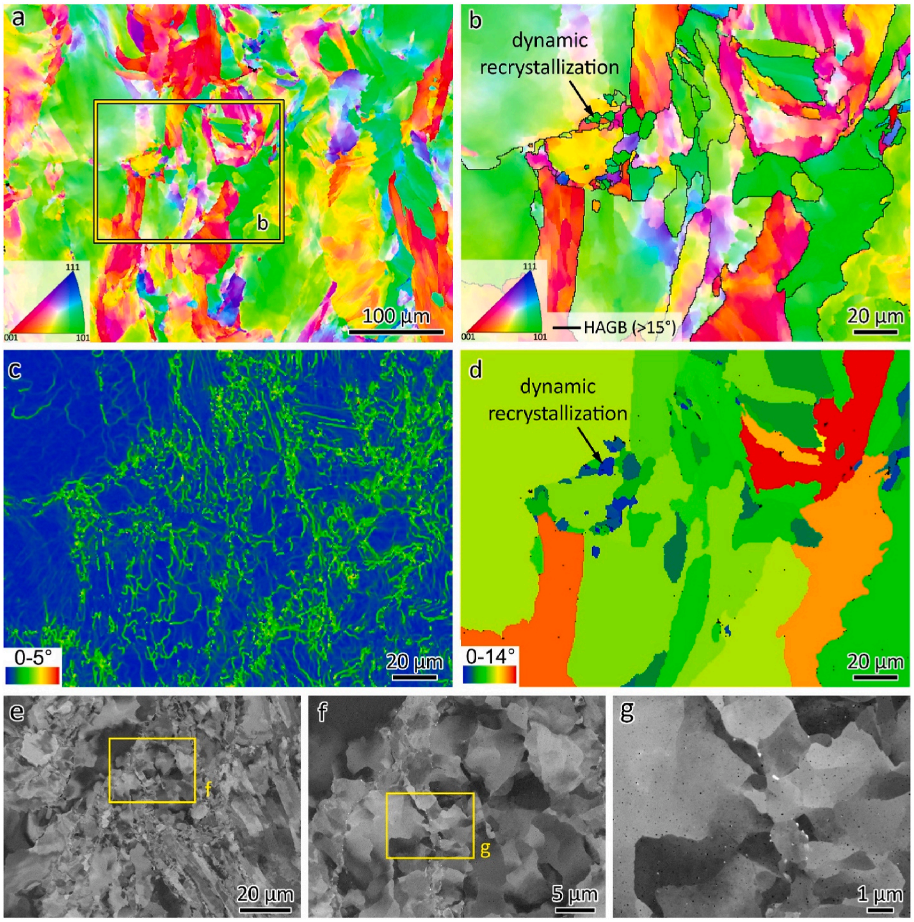

Fig. 13. Dynamic recrystallization induced refined grains in LPBF-processed 316L fractured at 800 °C. (a) EBSD orientation map, (b) a close up of the orientation map, (c) KAM map and (d) GOS map of (b), (e, f, g) SEM BSE images.

The cracks in creep consist of the following stages: (i) nucleation of cavities; (ii) growth of cavities, (iii) interlinkage of cavities, and (iv) crack propagation. The nucleation of cavities can be observed in Fig. 14 (d and e). The nucleation of cavities often happens at the grain boundaries which is because the accumulation of dislocations due to the slip causes stress concentration at the grain boundaries. The nanoscale ledges at the grain boundaries would be other sites for the nucleation of cavities, especially for the observation of the straight slim cracks. The triple junctions of the grain boundaries are also nucleation sites for creep cavities due to stress concentration. The left-top side of the crack in Fig. 14(e) is at the triple junction of the grain boundaries. The interlinkage of cavities can be seen in Fig. 14(d and e).

Fig. 15 summarizes the tensile deformation behaviors at different temperatures. It has been discovered that at −196 °C, there have been observations of deformation induced phase transformation and TWIP; between 25 °C and 125 °C, TWIP has been noted; at temperatures ranging from 550 °C to 600 °C, DSA has been observed; within the range of 700 °C–800 °C, creep at grain boundaries has been detected.; Additionally, dynamic recrystallization has been observed during testing at 800 °C.

5. Conclusions

(1) LPBF-processed 316L shows a good combination of high strength and ductility at room temperature. Deformation twinning was observed in the fractured samples. The yield strength is 609 MPa; the UTS is 722 MPa; the elongation is 62%;

(2) LPBF-processed 316L fractured at −196 °C shows an increased strength with good ductility due to TRIP and TWIP effect. The yield strength is 818 MPa; the UTS is 1349 MPa; the elongation is 39%;

(3) The formation of deformation twinning is significantly retarded when the testing temperature reaches 200 °C. At 400 °C, the elongation is decreased to 21%;

(4) At 550 °C and 600 °C, tensile curves with serrated flow were observed which is associated with DSA.

(5) Further increasing the testing temperature to 800 °C, the yield strength is decreased to 230 MPa and the UTS is decreased to 239 MPa with an elongation of 29%. Dynamic recrystallization was observed. The small elongation obtained at 800 °C results from the occurrence of high temperature creep.

CRediT authorship contribution statement

Wengang Zhai: Conceptualization, Data curation, Formal analysis, Investigation, Validation, Visualization, Writing – original draft, Writing – review & editing. **Fulin Liu:** Data curation, Formal analysis, Investigation. **Qingyuan Wang:** Resources. **Sharon Mui Ling Nai:** Formal analysis, Resources, Supervision. **Wei Zhou:** Conceptualization, Formal analysis, Methodology, Resources, Writing – review & editing.

Declaration of competing interest

The authors declare that they have no known competing financial interests or personal relationships that could have appeared to influence the work reported in this paper

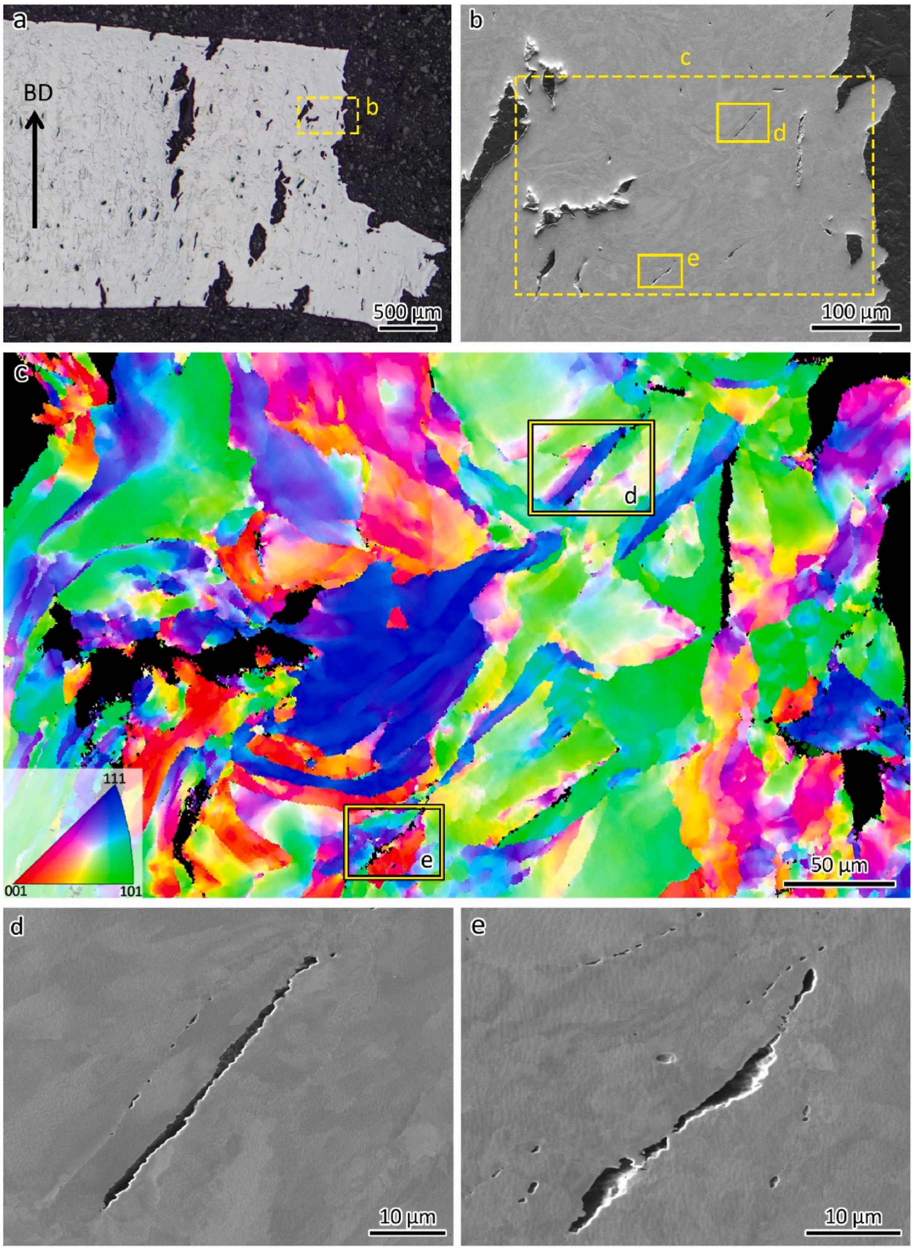

Fig. 14. Creep behavior of behaviour LPBF-processed 316L after fracture at 800 °C near the fracture point. (a) Optical image showing the creep cracks near the fracture point, (b) SEM image showing the close up of the creep cracks, (c) EBSD orientation map showing the microstructures near the fracture point, (d, e) SEM images showing the intergranular creep cracks. BD: building direction.

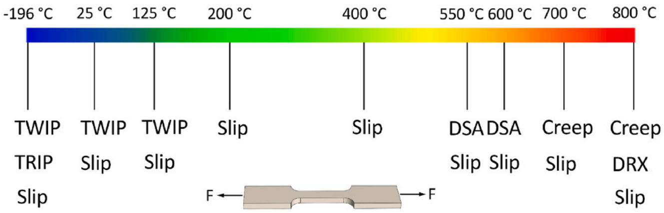

Fig. 15. Illustration showing the tensile deformation behaviors at different temperatures. Note: TWIP: twinning induced plasticity; TRIP: transformation induced plasticity; DSA: dynamic strain aging; DRX: dynamic recrystallization.

Data availability

"The raw/processed data required to reproduce these findings cannot be shared at this time as the data also forms part of an ongoing study. "

Acknowledgements

The authors acknowledge the support from the Singapore Institute of Manufacturing Technology for access to the Additive Innovation Centre and the support from Nanyang Technological University for access to the materials characterization facilities. The authors thank Dr Kaiqiang Wu from Nanyang Technological University for the assistance with the XRD measurement.

References

[1] D. Molnár, X. Sun, S. Lu, W. Li, G. Engberg, L. Vitos, Effect of temperature on the stacking fault energy and deformation behaviour in 316L austenitic stainless steel, Mater. Sci. Eng., A 759 (2019) 490–497, https://doi.org/10.1016/j.msea.2019.05.079.

[2] J.J. Lewandowski, M. Seifi, Metal additive manufacturing: a review of mechanical properties, Annu. Rev. Mater. Res. 46 (1) (2016) 151–186, https://doi.org/10.1146/annurev-matsci-070115-032024.

[3] L. Zhang, Z. Hu, M.Y. Wang, S. Feih, Hierarchical sheet triply periodic minimal surface lattices: design, geometric and mechanical performance, Mater. Des. (2021) 209, https://doi.org/10.1016/j.matdes.2021.109931.

[4] W. Zhai, P. Wang, F.L. Ng, W. Zhou, S.M. Ling Nai, J. Wei, Hybrid manufacturing of γ-TiAl and Ti–6Al–4V bimetal component with enhanced strength using electron beam melting, Compos. B Eng. 207 (2021) 108587, https://doi.org/10.1016/j.compositesb.2020.108587.

[5] L. Xu, Z. Chai, X. Zhang, B. Peng, W. Zhou, X. Chen, A new approach to improve strength and ductility of laser powder deposited Inconel 718 thin-wall structure, Mater. Sci. Eng., A 855 (2022), https://doi.org/10.1016/j.msea.2022.143871.

[6] W. Zhai, N. Wu, W. Zhou, Effect of interpass temperature on wire arc additive manufacturing using high-strength metal-cored wire, Metals 12 (2) (2022) 212, https://doi.org/10.3390/met12020212.

[7] D. Kong, C. Dong, X. Ni, L. Zhang, J. Yao, C. Man, X. Cheng, K. Xiao, X. Li, Mechanical properties and corrosion behavior of selective laser melted 316L stainless steel after different heat treatment processes, J. Mater. Sci. Technol. 35 (7) (2019) 1499–1507, https://doi.org/10.1016/j.jmst.2019.03.003.

[8] L. Liu, Q. Ding, Y. Zhong, J. Zou, J. Wu, Y.-L. Chiu, J. Li, Z. Zhang, Q. Yu, Z. Shen, Dislocation network in additive manufactured steel breaks strength–ductility trade-off, Mater. Today 21 (4) (2018) 354–361, https://doi.org/10.1016/j.mattod.2017.11.004.

[9] W. Zhai, W. Zhou, S.M.L. Nai, Grain refinement and strengthening of 316L stainless steel through addition of TiC nanoparticles and selective laser melting, Mater. Sci. Eng., A 832 (2022) 142460, https://doi.org/10.1016/j.msea.2021.142460.

[10] F. Wei, B. Cheng, P. Kumar, P. Wang, J.J. Lee, H.L. Seng, K.H. Cheong, K.B. Lau, C. C. Tan, A comparative study of additive manufactured and wrought SS316L: pre-existing dislocations and grain boundary characteristics, Mater. Sci. Eng., A 833 (2022) 142546, https://doi.org/10.1016/j.msea.2021.142546.

[11] M. Shamsujjoha, S.R. Agnew, J.M. Fitz-Gerald, W.R. Moore, T.A. Newman, High strength and ductility of additively manufactured 316L stainless steel explained, Metall. Mater. Trans. 49 (7) (2018) 3011–3027, https://doi.org/10.1007/s11661-018-4607-2.

[12] Y.J. Yin, J.Q. Sun, J. Guo, X.F. Kan, D.C. Yang, Mechanism of high yield strength and yield ratio of 316 L stainless steel by additive manufacturing, Mater. Sci. Eng., A 744 (2019) 773–777, https://doi.org/10.1016/j.msea.2018.12.092.

[13] Q. Chao, V. Cruz, S. Thomas, N. Birbilis, P. Collins, A. Taylor, P.D. Hodgson, D. Fabijanic, On the enhanced corrosion resistance of a selective laser melted austenitic stainless steel, Scripta Mater. 141 (2017) 94–98, https://doi.org/10.1016/j.scriptamat.2017.07.037.

[14] X. Lou, M.A. Othon, R.B. Rebak, Corrosion fatigue crack growth of laser additively-manufactured 316L stainless steel in high temperature water, Corrosion Sci. 127 (2017) 120–130, https://doi.org/10.1016/j.corsci.2017.08.023.

[15] W. Zhai, W. Zhou, Z. Zhu, S.M.L. Nai, Selective laser melting of 304L and 316L stainless steels: a comparative study of microstructures and mechanical properties, Steel Res. Int. 93 (7) (2022) 2100664, https://doi.org/10.1002/srin.202100664.

[16] K. Saeidi, L. Kvetková, F. Lofaj, Z. Shen, Austenitic stainless steel strengthened by the in situ formation of oxide nanoinclusions, RSC Adv. 5 (27) (2015) 20747–20750, https://doi.org/10.1039/c4ra16721j.

[17] S.G. Chowdhury, S. Das, P.K. De, Cold rolling behaviour and textural evolution in AISI 316L austenitic stainless steel, Acta Mater. 53 (14) (2005) 3951–3959, https://doi.org/10.1016/j.actamat.2005.05.006.

[18] V.S.A. Challa, X.L. Wan, M.C. Somani, L.P. Karjalainen, R.D.K. Misra, Strain hardening behavior of phase reversion-induced nanograined/ultrafine-grained (NG/UFG) austenitic stainless steel and relationship with grain size and deformation mechanism, Mater. Sci. Eng., A 613 (2014) 60–70, https://doi.org/10.1016/j.msea.2014.06.065.

[19] S. Huang, W. Li, S. Lu, F. Tian, J. Shen, E. Holmström, L. Vitos, Temperature dependent stacking fault energy of FeCrCoNiMn high entropy alloy, Scripta Mater. 108 (2015) 44–47, https://doi.org/10.1016/j.scriptamat.2015.05.041.

[20] G. Muhamed, S. Gündüz, M. Erden, D. Taştemur, Dynamic strain aging behaviour in AISI 316L austenitic stainless steel under as-received and as-welded conditions, Metals 7 (9) (2017) 362, https://doi.org/10.3390/met7090362.

[21] C. Wang, X. Lin, L. Wang, S. Zhang, W. Huang, Cryogenic mechanical properties of 316L stainless steel fabricated by selective laser melting, Mater. Sci. Eng., A 815 (2021) 141317, https://doi.org/10.1016/j.msea.2021.141317.

[22] G.M. Karthik, E.S. Kim, P. Sathiyamoorthi, A. Zargaran, S.G. Jeong, R. Xiong, S. H. Kang, J.-W. Cho, H.S. Kim, Delayed deformation-induced martensite transformation and enhanced cryogenic tensile properties in laser additive manufactured 316L austenitic stainless steel, Addit. Manuf. 47 (2021), https://doi.org/10.1016/j.addma.2021.102314.

[23] M.S. Pham, B. Dovgyy, P.A. Hooper, Twinning induced plasticity in austenitic stainless steel 316L made by additive manufacturing, Mater. Sci. Eng., A 704 (2017) 102–111, https://doi.org/10.1016/j.msea.2017.07.082.

[24] A.-C. Yeh, K.-W. Lu, C.-M. Kuo, H.-Y. Bor, C.-N. Wei, Effect of serrated grain boundaries on the creep property of Inconel 718 superalloy, Mater. Sci. Eng., A 530 (2011) 525–529, https://doi.org/10.1016/j.msea.2011.10.014.

[25] N.D. Stepanov, D.G. Shaysultanov, N.Y. Yurchenko, S.V. Zherebtsov, A.N. Ladygin, G.A. Salishchev, M.A. Tikhonovsky, High temperature deformation behavior and dynamic recrystallization in CoCrFeNiMn high entropy alloy, Mater. Sci. Eng., A 636 (2015) 188–195, https://doi.org/10.1016/j.msea.2015.03.097.

[26] W. Zhai, W. Zhou, S.M.L. Nai, In-situ formation of TiC nanoparticles in selective laser melting of 316L with addition of micronsized TiC particles, Mater. Sci. Eng., A 829 (2022) 142179, https://doi.org/10.1016/j.msea.2021.142179.

[27] S. Gao, Z. Hu, M. Duchamp, P.S.S.R. Krishnan, S. Tekumalla, X. Song, M. Seita, Recrystallization-based grain boundary engineering of 316L stainless steel produced via selective laser melting, Acta Mater. 200 (2020) 366–377, https://doi.org/10.1016/j.actamat.2020.09.015.

[28] T. Voisin, J.-B. Forien, A. Perron, S. Aubry, N. Bertin, A. Samanta, A. Baker, Y. M. Wang, New insights on cellular structures strengthening mechanisms and thermal stability of an austenitic stainless steel fabricated by laser powder-bed-fusion, Acta Mater. 203 (2021) 116476, https://doi.org/10.1016/j.actamat.2020.11.018.

[29] Z. Sun, X. Tan, S.B. Tor, W.Y. Yeong, Selective laser melting of stainless steel 316L with low porosity and high build rates, Mater. Des. 104 (2016) 197–204, https://doi.org/10.1016/j.matdes.2016.05.035.

[30] T.H. Man, T.W. Liu, D.H. Ping, T. Ohmura, TEM investigations on lath martensite substructure in quenched Fe-0.2C alloys, Mater. Char. 135 (2018) 175–182, https://doi.org/10.1016/j.matchar.2017.11.039.

[31] G.B. Olson, M. Cohen, A mechanism for the strain-induced nucleation of martensitic transformations, J. Less Common Metals 28 (1) (1972) 107–118, https://doi.org/10.1016/0022-5088(72)90173-7.

[32] C.X. Huang, G. Yang, Y.L. Gao, S.D. Wu, S.X. Li, Investigation on the nucleation mechanism of deformation-induced martensite in an austenitic stainless steel under severe plastic deformation, J. Mater. Res. 22 (3) (2011) 724–729, https://doi.org/10.1557/jmr.2007.0094.

[33] C. Zhang, D. Juul Jensen, T. Yu, Microstructure and texture evolution during cold rolling of 316L stainless steel, Metall. Mater. Trans. 52 (9) (2021) 4100–4111, https://doi.org/10.1007/s11661-021-06367-6.

[34] W. Abuzaid, H. Sehitoglu, Critical resolved shear stress for slip and twin nucleation in single crystalline FeNiCoCrMn high entropy alloy, Mater. Char. 129 (2017) 288–299, https://doi.org/10.1016/j.matchar.2017.05.014.

[35] D. Riabov, A. Leicht, J. Ahlström, E. Hryha, Investigation of the strengthening mechanism in 316L stainless steel produced with laser powder bed fusion, Mater. Sci. Eng., A 822 (2021), https://doi.org/10.1016/j.msea.2021.141699.

[36] C. Zhang, D. Juul Jensen, T. Yu, Effects of initial 3D printed microstructures on subsequent microstructural evolution in 316L stainless steel, Acta Mater. 242 (2023), https://doi.org/10.1016/j.actamat.2022.118481.

[37] Y. Zhang, J.P. Liu, S.Y. Chen, X. Xie, P.K. Liaw, K.A. Dahmen, J.W. Qiao, Y. L. Wang, Serration and noise behaviors in materials, Prog. Mater. Sci. 90 (2017) 358–460, https://doi.org/10.1016/j.pmatsci.2017.06.004.

[38] F. Bakare, L. Schieren, B. Rouxel, L. Jiang, T. Langan, A. Kupke, M. Weiss, T. Dorin, The impact of L12 dispersoids and strain rate on the Portevin-Le-Chatelier effect and mechanical properties of Al–Mg alloys, Mater. Sci. Eng., A 811 (2021) 141040, https://doi.org/10.1016/j.msea.2021.141040.

[39] Z. Zhu, F.L. Ng, H.L. Seet, W. Lu, C.H. Liebscher, Z. Rao, D. Raabe, S. Mui Ling Nai, Superior mechanical properties of a selective-laser-melted AlZnMgCuScZr alloy enabled by a tunable hierarchical microstructure and dual-nanoprecipitation, Mater. Today 52 (2022) 90–101, https://doi.org/10.1016/j.mattod.2021.11.019.

[40] Z. Hu, Y. Qi, X. Nie, H. Zhang, H. Zhu, The Portevin-Le Chatelier (PLC) effect in an Al-Cu aluminum alloy fabricated by selective laser melting, Mater. Char. 178 (2021) 111198, https://doi.org/10.1016/j.matchar.2021.111198.

[41] S. Lee, Y. Estrin, B.C. De Cooman, Effect of the strain rate on the TRIP–TWIP transition in austenitic Fe-12 pct Mn-0.6 pct C TWIP steel, Metall. Mater. Trans. 45 (2) (2013) 717–730, https://doi.org/10.1007/s11661-013-2028-9.

[42] R.J. Williams, J. Al-Lami, P.A. Hooper, M.-S. Pham, C.M. Davies, Creep deformation and failure properties of 316 L stainless steel manufactured by laser powder bed fusion under multiaxial loading conditions, Addit. Manuf. 37 (2021), https://doi.org/10.1016/j.addma.2020.101706.

[43] L.A. Ávila Calderón, B. Rehmer, S. Schriever, A. Ulbricht, L. Agudo Jácome, K. Sommer, G. Mohr, B. Skrotzki, A. Evans, Creep and creep damage behavior of stainless steel 316L manufactured by laser powder bed fusion, Mater. Sci. Eng., A 830 (2022), https://doi.org/10.1016/j.msea.2021.142223.

[44] X. Zhang, C.P. Carter, Y. Satapathy, A. Tekawade, J.-S. Park, P. Kenesei, M. Li, Understanding creep behaviors of additively manufactured 316L stainless steel via void characterization, Mater. Res. Lett. 11 (10) (2023) 806–813, https://doi.org/10.1080/21663831.2023.2244969.